ELSEVIER

Journal of Crystal Growth 234 (2002) 47–62

JOURNAL OF CRYSTAL GROWTH

www.elsevier.com/locate/jcrysgro

Controlling transport phenomena in the Czochralski crystal growth process☆

M. Gunzburger[a], E. Ozugurlu[a,b,*], J. Turner[c], H. Zhang[d]

[a] Department of Mathematics, Iowa State University, Ames, IA 50011-2064, USA
[b] Faculty of Engineering and Science, Sabanci University, Orhanli, Tuzla 81474, Istanbul, Turkey
[c] Department of Mathematics, Arizona State University, Tempe, AZ 85287-1804, USA
[d] Department of Mechanical Engineering, State University of New York, Stony Brook, NY 11794-2300, USA

Received 29 March 2001; accepted 25 July 2001
Communicated by J.J. Derby

Abstract

A mathematical formulation and computational techniques are presented to describe optimal control and design strategies for the suppression of turbulent motions in the melt and the minimization of temperature gradients in the crystal in Czochralski crystal growth processes. The methodologies developed can be used to test control mechanisms, design parameters, and optimization objectives to determine their effectiveness in improving the processes. They can also be used to effect such improvements by systematically determining optimal values of the design parameters. The controls or design parameters considered include applied magnetic fields, temperature gradients along the side wall of the crucible, and crucible and crystal rotation rates. The results show that applied magnetic fields can be very effective in reducing velocity perturbations in the melt, while side wall temperature gradients are less effective and crucible and crystal rotation rates are ineffective. The results also show that applied magnetic field and crucible and rotation rates are ineffective in reducing temperature gradients in the crystal or in the melt. © 2002 Elsevier Science B.V. All rights reserved.

Keywords: A1. Computer simulation; A1. Magnetic fields; A2. Czochralski method; A2. Growth from melt; A2. Magnetic field assisted Czochralski method; A2. Optimal control of growth process

1. Introduction

During the past several decades, three different types of crystal growth techniques have been developed, namely, vapor, melt, and solution [1]. Nevertheless, the melt growth technique, i.e., the *Czochralski* (Cz) *process*, has dominated the production of single crystals for most of the materials used in the microelectronics industry. However, in spite of the popularity of the Cz

---

☆This work was performed with the support of the Air Force Office of Scientific Research under grant number F49620-95-1-0407.

*Corresponding author. Faculty of Engineering and Science, Sabanci University, Orhanli, Tuzla 81474, Istanbul, Turkey. Tel.: +90-216-483-9000; fax: +90-216-483-9550.

E-mail address: ozugurlu@maria.la.asu.edu (E. Ozugurlu).

PII: S0022-0248(01)01635-9

method, there remain many limitations. For example, without an externally applied magnetic field, the melt motion in many commercial processes that use the Cz method is turbulent and involves large scale motions. Heat flux fluctuations from the melt to the crystal produce a cycle of crystallization and remelting at the interface. This cycle produces dislocations and other microscopic defects in the crystal. Experiments on *magnetic Czochralski* (MCz) growth have shown that the temperature fluctuations and erratic doping striations are suppressed by the application of a magnetic field [2]. In fact, the most important benefit of the magnetic field is that it controls impurities and inhomogeneities at microscopic levels by producing better conditions in the vicinity of the melt/crystal interface. Nevertheless, the use of MCz processes for the industrial production of crystals is still very limited because of its cost, as well as the limited understanding of when and how the magnetic field stabilizes the melt. Since MCz is expected to become the future technology for materials that are difficult to grow, particularly at high and ultra-high pressures, as well as the industry norm for the growth of large-size crystals, our current focus is on introducing magnetic effects into an existing Cz model.

Here, we present a systematic approach to the control or optimization of the MCz crystal growth process. Even though the fundamentals of individual transport processes within the Cz process may appear to be simple, their interactions are rather complex. Thus, the notion of controlling the process is a nontrivial matter. In particular, it is seldom obvious which design parameters are effective for use in achieving a specific objective. Thus, our goal is to develop a methodology that can be used to test, through computational experiments, the effectiveness of design objectives and parameters. We also want this methodology to be useful for the actual design of improved crystal growth processes. To this end, we show that some design parameters, e.g., the strength of an applied magnetic field, can be very effective in improving some aspects of the MCz crystal growth process.

We first investigate the effects on the melt flow velocity that occur as a result of various actions that can be applied, using design parameters such as the strength of an applied magnetic field, the temperature along the boundaries, and the crystal and crucible rotation rates. We also investigate the effect of these design parameters on the temperature gradient in the crystal during the growth process.

2. Mathematical model for the MCz process

2.1. Governing equations

A sketch of the physical domain used for our calculations is given in Fig. 1. The basic equations governing the melt in a MCz crystal growth process are a coupled magnetohydrodynamics (MHD) system. This system is composed of the conservation equations for fluid momentum, mass, and energy, Maxwell's equations, and Ohm's law for a medium in motion. The conservation equations for the melt, in primitive variables, are given by

$$\rho\left(\frac{\partial \mathbf{u}}{\partial t} + \mathbf{u}\cdot\nabla\mathbf{u}\right) - \mu\Delta\mathbf{u} + \nabla p = \mathbf{F}_{\mathrm{b}} + \mathbf{F}_{\mathrm{m}}, \tag{1}$$

$$\nabla\cdot\mathbf{u} = 0, \tag{2}$$

$$\rho c_p\left(\frac{\partial T}{\partial t} + \mathbf{u}\cdot\nabla T\right) = \kappa\Delta T, \tag{3}$$

where $\rho, \mathbf{u}, p$, and T are the fluid density, velocity vector, pressure, and temperature, respectively.

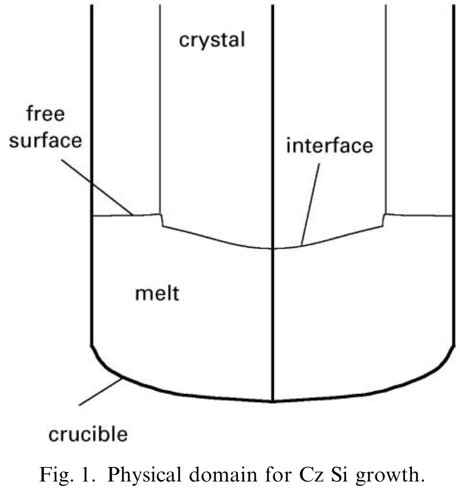

Fig. 1. Physical domain for Cz Si growth.

The parameters μ, c_p, and κ appearing in the above equations are the fluid viscosity, specific heat capacity at constant pressure, and thermal conductivity, respectively. $\mathbf{F}_{\mathrm{b}}$ is the buoyancy force, which is modeled in the Boussinesq approximation by [3,4]

$$\mathbf{F}_{\mathrm{b}} = -(\rho - \rho_0) g \mathbf{e}_z = \rho_0 \beta (T - T_{\mathrm{f}}) g \mathbf{e}_z, \tag{4}$$

where $\mathbf{e}_z$ denotes the unit vector in the z direction so that the gravitational acceleration is represented by the constant vector $-g\mathbf{e}_z$. In Eqs. (1)–(4), we are assuming that the variations in the density in the melt are negligible, i.e., the fluid density $\rho = \rho_0$ is constant, except in the body force term $\mathbf{F}_{\mathrm{b}}$, where the density is taken to be $\rho = \rho_0(1 - \beta(T - T_{\mathrm{f}}))$. Here, ρ_0 is the melt density, T_{f} is a reference temperature which we choose to be the melt freezing temperature, and β is the thermal expansion coefficient. $\mathbf{F}_{\mathrm{m}}$ denotes the Lorentz force induced by the magnetic field on the moving fluid; it can dampen convection and can thus produces better flow conditions in the melt.

For magnetohydrodynamic applications, Maxwell's equations and Ohm's law are given by [5]

$$\mathbf{j} = \sigma(\mathbf{E} + \mathbf{u} \times \mathbf{B}), \tag{5}$$

$$\nabla \times \mathbf{B} = \mu_{\mathrm{e}} \mathbf{j}, \tag{6}$$

$$\nabla \cdot \mathbf{B} = 0, \tag{7}$$

$$\nabla \times \mathbf{E} = -\frac{\partial \mathbf{B}}{\partial t}, \tag{8}$$

where σ is electric conductivity of the melt, $\mathbf{B}$ is the magnetic induction, $\mathbf{j}$ is the induced current density, $\mathbf{E}$ is the electric field, and μ_{e} is the magnetic permeability of the melt. System (5)–(8) may be combined to yield

$$\frac{\partial \mathbf{B}}{\partial t} = \frac{1}{\sigma \mu_{\mathrm{e}}} \Delta \mathbf{B} + \nabla \times (\mathbf{u} \times \mathbf{B}) \quad \text{and} \quad \nabla \cdot \mathbf{B} = 0. \tag{9}$$

We nondimensionalize utilizing the following scalings: length b, velocity v/b, pressure $\rho v^2/b^2$, time b^2/v, and magnetic induction $\mu_{\mathrm{e}} H_0$, where $v = \mu/\rho_0$ is the kinematic viscosity and H_0 is the magnitude of the applied magnetic field. We set $\Theta = (T - T_{\mathrm{f}})/(T_{\mathrm{c}} - T_{\mathrm{f}})$, where T_{c} is the constant temperature at the bottom crucible wall. Using these scalings, the nondimensionalized governing equations for flow and heat transfer in the melt are given by

$$\frac{\partial \mathbf{u}}{\partial t} + (\mathbf{u} \cdot \nabla)\mathbf{u} + \nabla p - \Delta \mathbf{u} = \mathrm{Gr}\, \Theta \mathbf{e}_z + \mathbf{F}_{\mathrm{m}}, \tag{10}$$

$$\nabla \cdot \mathbf{u} = 0, \tag{11}$$

$$\frac{\partial \Theta}{\partial t} + \mathbf{u} \cdot \nabla \Theta = \frac{1}{\mathrm{Pr}} \Delta \Theta, \tag{12}$$

where the components of $\mathbf{F}_{\mathrm{m}}$ in the x, r, and θ-directions are, respectively, given by

$$F_x = 0, \quad F_r = -\frac{\mathrm{Ha}^2 \sigma}{\sigma_{\mathrm{m}}} v, \quad F_\theta = -\mathrm{Ha}^2 \frac{\partial \Psi}{\partial x}. \tag{13}$$

We solve the electric current stream function equation (ECSFE) instead of for the electric potential. The primary advantage of using the stream function equation is the simplicity in implementating boundary conditions. The boundary conditions for the potential equation are much more complicated on curvilinear walls. Then, (ECSFE) can be written as

$$\frac{\partial}{\partial x}\left(\frac{\sigma_{\mathrm{m}}}{\sigma} \frac{1}{r} \frac{\partial \Psi}{\partial x}\right) + \frac{\partial}{\partial x}\left(\frac{\sigma_{\mathrm{m}}}{\sigma} \frac{1}{r} \frac{\partial \Psi}{\partial r}\right) = \frac{\partial w}{\partial x}. \tag{14}$$

The magnetic field is governed by

$$\frac{\partial \mathbf{B}}{\partial t} = \frac{1}{\mathrm{Re}_{\mathrm{m}}} \Delta \mathbf{B} + \nabla \times (\mathbf{u} \times \mathbf{B}), \ \nabla \cdot \mathbf{B} = 0 \tag{15}$$

and the temperature in the crystal is governed by

$$\frac{\partial \Theta}{\partial t} = \kappa_{\mathrm{s}} \Delta \Theta. \tag{16}$$

In these equations, $\mathrm{Gr} = g\beta b^3 (T_{\mathrm{c}} - T_{\mathrm{f}})/v^2$, $\mathrm{Pr} = v c_{\mathrm{p}}/\kappa$, $\mathrm{Re}_{\mathrm{m}} = \mu_{\mathrm{e}} \sigma v$, $\mathrm{Ha} = \mu_{\mathrm{e}} H_0 b \sqrt{\sigma/\mu}$, and κ_{s} denote the dimensionless Grashof number, Prandtl number, magnetic Reynolds number, Hartmann number, and nondimensional thermal diffusivity, respectively.

Initial conditions can be specified on the melt velocity and temperature and the crystal temperature.

2.2. Interface and boundary conditions

We restrict attention to axially symmetric melt flows described in terms of cylindrical coordinates. Note that for computational reasons, an enclosing top surface has also been employed.

We implemented the boundary conditions easily by using the stream function equation. The boundary condition for Eq. (14) is

$$\nabla \Psi = 0. \tag{17}$$

The evolving crystal/melt and free surface/melt interfaces have a profound effect on the quality of the grown crystal. Thus, in order to accurately capture this evolution, we model the melt region by

$$\Omega_{\mathrm{m}} = \{(r,z) | 0 \leqslant r \leqslant r_1, \; z_0(r) \leqslant z \leqslant Z(r,t)\}, \tag{18}$$

where $Z(r,t)$ is defined by

$$Z(r,t) = \begin{cases} Z_1(r,t), & 0 \leqslant r \leqslant r^*(t), \\ Z_2(r,t), & r^*(t) < r \leqslant b. \end{cases} \tag{19}$$

$z_0(r)$ is the dimensionless shape function for the bottom of the crucible. $Z(r,t)$ is the dimensionless height of the moving interfaces, with $Z_1(r,t)$ representing the crystal/melt interface and $Z_2(r,t)$ the encapsulant/melt interface; $r^*(t)$ is the triple point where the melt, crystal, and encapsulant meet. The parameter b is thus chosen to be the distance from the axis of symmetry to the vertical wall of the crucible. Note that, in this setting, we are modeling the solidification of a pure substance with a fixed fusion temperature T_{f} and thus we assume that the solid and liquid phases are separated by a sharp interface given by $s(z,r,t) = Z_1(r,t) - z = 0$. The energy balance at the crystal/melt interface defines its movement; it is governed by [6]

$$\frac{\partial Z_1}{\partial t} - u_{\mathrm{p}}(t) = \frac{\mathrm{Ste}}{\mathrm{Pr}} \left(\frac{\kappa_{\mathrm{s}}}{\kappa_{\mathrm{m}}} \frac{\partial \Theta_{\mathrm{s}}}{\partial n} - \frac{\partial \Theta_{\mathrm{m}}}{\partial n} \right) \left(1 + \left(\frac{\partial Z_1}{\partial r} \right)^2 \right), \tag{20}$$

where $u_{\mathrm{p}}(t)$ is the pull rate, $\mathrm{Ste} = C_{\mathrm{ps}}(T_{\mathrm{c}} - T_{\mathrm{f}})/h_{\mathrm{f}}$ is the Stefan number of the melt, h_{f} is the latent heat, and the subscripts s and m refer to crystal and melt regions. This equation is based on the assumption that the crystal and melt are not separated at the triple point.

Denoting the free-surface position as $z = Z_2(r,t)$, the height of the free surface can be determined by solving

$$\frac{\partial^2 Z_2/\partial r^2}{(1 + (\partial Z_2/\partial r)^2)^{3/2}} + \frac{\partial Z_2/\partial r}{r(1 + (\partial Z_2/\partial r)^2)^{1/2}} = \mathrm{Bo}(Z_2 - \lambda), \tag{21}$$

where $\mathrm{Bo} = \rho g b^2/\sigma_{\mathrm{s}}$ is the Bond number, σ_{s} is the surface tension, and the parameter λ can be calculated from the melt conservation constraint

$$\int_0^{\mathrm{Rr}} Z_1 r \, \mathrm{d}r + \int_{\mathrm{Rr}}^1 Z_2 r \, \mathrm{d}r = \frac{V_{\mathrm{m}}(t)}{2\pi}, \tag{22}$$

where $V_{\mathrm{m}}(t)$ is the volume of the melt and $\mathrm{Rr} = r_{\mathrm{s}}/b$ is the radius ratio where r_{s} is the radial co-ordinate of the crystal.

There are two boundary conditions needed to solve for the shape of the encapsulant/melt interface. At the triple point, the meniscus is considered to be pinned to the edge of the crystal, and at the junction between the encapsulant and crucible wall, a 90-deg contact angle is assumed in view of the weak influence of the shape of the crucible meniscus on heat transfer.

Additional boundary conditions for the problem under consideration include the following: at the crystal/melt interface,

$$u = u_{\mathrm{int}}, \quad v = v_{\mathrm{int}}, \quad w = \mathrm{Re}_{\mathrm{s}} r, \quad \Theta = 0, \tag{23}$$

at the encapsulant/melt interface,

$$u = \frac{\partial Z_2}{\partial t} + v \frac{\partial Z_2}{\partial r}, \quad \frac{\partial v}{\partial n} - \frac{\partial u}{\partial \tau} = \frac{\mathrm{Ma}}{\mathrm{Pr}} \frac{\partial \Theta}{\partial n}, \quad - \frac{\kappa_{\mathrm{fs}}}{\kappa_{\mathrm{s}}} \frac{\partial \Theta_{\mathrm{fs}}}{\partial n} = \mathrm{Bi}_{\mathrm{fs}}(\Theta_{\mathrm{fs}} - \Theta_{\mathrm{a}}), \tag{24}$$

at the bottom and side wall of the crucible,

$$u = v = 0, \quad w = \mathrm{Re}_{\mathrm{c}}\, r, \quad \Theta = \Theta_{\mathrm{w}}, \tag{25}$$

at the top and side wall of the crystal,

$$- \frac{\partial \Theta_{\mathrm{s}}}{\partial n} = \mathrm{Bi}_{\mathrm{s}}(\Theta_{\mathrm{s}} - \Theta_{\mathrm{a}}), \tag{26}$$

where $\mathrm{Re}_{\mathrm{s}} = \Omega_{\mathrm{s}} b^2/v$ and $\mathrm{Re}_{\mathrm{c}} = \Omega_{\mathrm{c}} b^2/v$ are the crystal and crucible rotation Reynolds numbers, respectively, Ω_{s} and Ω_{c} are the rotation rates for the crystal and crucible, respectively, the subscript fs refers to the free surface, $\mathrm{Ma} = (\partial \sigma_{\mathrm{s}}/\partial T)(T_{\mathrm{c}} - T_{\mathrm{f}}) b/\mu\alpha$ is the Marangoni number, $\Theta_{\mathrm{w}}, \Theta_{\mathrm{s}}$, and Θ_{a} are the dimensionless crucible wall temperature, crystal boundary temperature, and ambient temperatures, respectively, and u_{int} and

v_{int} are the interface velocity components in the z and r directions, respectively. Since the objective of our paper is to develop a control algorithm for quasi-state cases, the interface velocities will not be presented here. However, they are important in transient calculations; we calculated them but did not save them in simulations.

Since we focused on controlling the melt flow with a magnetic field, we used the simplified radiation model which was developed by Prasad et al. [7]. It is based on the method of discrete exchange factor (DEF) [8]. The radiative heat loss has been considered from the side wall of the crystal and the melt free surface with radiation Biot number $\mathrm{Bi} = \varepsilon\sigma(T^2 + T_{\mathrm{a}}^2)(T + T_{\mathrm{a}})b/\kappa_{\mathrm{s}}$, where ε is the emissivity and T_{a} is the ambient temperature.

3. Modeling MCz control

There are many opportunities for introducing optimal control strategies into crystal growth processes. Ultimately, we want to apply control strategies in order to improve, either directly or indirectly, the quality of the crystal. Applying control strategies that directly affect crystal properties is very difficult. Therefore, as a first step in applying systematic optimal control strategies to crystal growth processes, we will apply control strategies that only indirectly affect crystal properties.

Specifically, we will examine three different objectives for control along with, at first, two different control mechanisms. The first objective is to minimize the vorticity in the melt region; this is an effort directed at lessening large-scale turbulent motions inside the melt and to indirectly minimize oscillations in the melt–crystal interface. The second objective is to minimize the gradient of the temperature in the melt; this is an effort directed at lessening temperature variations in the melt. The third objective is to minimize the gradient of the temperature in the crystal; this is an effort directed at indirectly lessening the presence of residual stresses in the crystal. The two controls we will employ are the strength of the applied magnetic field and the temperature on the side wall of the crucible. For our nondimensionalized model, the strength of the applied field enters only through the Hartmann number; thus, the Hartmann number is one of our control parameters. The temperature on the side wall of the crucible is assumed to be linear in the height z; of course, the temperature at the bottom of the side wall should be the same as the temperature at the bottom of the crucible which is assumed to be constant, i.e., $T = T_{\mathrm{c}}$ along the bottom of the crucible. Thus, on the side wall of the crucible we have that

$$\Theta(z) = 1 + \xi\left(\frac{z - z_{\mathrm{b}}}{z_{\mathrm{L}} - z_{\mathrm{b}}}\right), \tag{27}$$

where $z_{\mathrm{b}} = z_0(b)$ and z_{L} are the dimensionless heights at the bottom and top of the side wall of the crucible. Thus, the slope factor ξ is a second control parameter at our disposal. Note that if $\xi < -1$, then the temperature on the side wall at the top of the crucible will be lower than the melting temperature of the melt. This is, of course, unacceptable, since it would cause the melt to solidify at the crucible wall. Therefore, we impose the constraint $\xi \geqslant -1$ in our optimization studies. See Fig. 2 for the results of a simulation with $\xi = -1.1$; the figure gives level curves of the temperature in the melt and crystal. Note, for this value of ξ, the small region of solidified melt at the top of the side wall of the crucible.

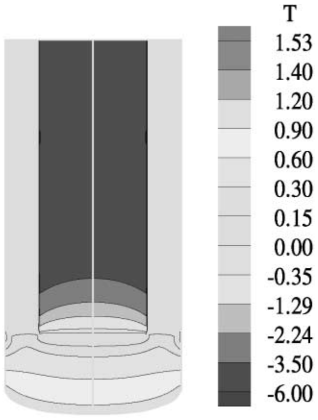

Fig. 2. Nondimensionalized temperature in the melt and crystal for a linear crucible side wall temperature profile with $\xi = -1.1$. Note the small region of solidified melt adjacent to the top of the crucible wall.

We now give a mathematical description of the optimal control problems we consider. Here, $(0, T)$ denotes the (nondimensionalized) time interval over which one wants to exercise control, Ω_{m} denotes the melt region, and Ω_{c} denotes the crystal region. The first optimization problem is given by: *final optimal values of* Ha *and* ξ *such that*

$$\mathscr{J}_1(\mathrm{Ha}, \xi) = \int_0^T \int_{\Omega_{\mathrm{m}}} |\nabla \times \mathbf{u}|^2 \, \mathrm{d}\Omega \, \mathrm{d}t \tag{28}$$

is minimized, where $\mathbf{u}(t, r, z;\ \mathrm{Ha}, \xi)$ *satisfies governing system* (10)–(16) *along with initial conditions and the boundary and interface conditions of* Section 2.2.

The second optimization problem is given by: *final optimal values* Ha *and* ξ *such that*

$$\mathscr{J}_2(\mathrm{Ha}, \xi) = \int_0^T \int_{\Omega_{\mathrm{m}}} |\nabla T|^2 \, \mathrm{d}\Omega \, \mathrm{d}t \tag{29}$$

is minimized, where $T(t, r, z;\ \mathrm{Ha}, \xi)$ *satisfies governing system* (10)–(16) *along with initial conditions and the boundary and interface conditions of* Section 2.2.

The third optimization problem is given by: *final optimal values of* Ha *and* ξ *such that*

$$\mathscr{J}_3(\mathrm{Ha}, \xi) = \int_0^T \int_{\Omega_{\mathrm{c}}} |\nabla T|^2 \, \mathrm{d}\Omega \, \mathrm{d}t \tag{30}$$

is minimized, where $T(t, r, z;\ \mathrm{Ha}, \xi)$ *satisfies governing system* (10)–(16) *along with initial conditions and the boundary and interface conditions of* Section 2.2.

These represent nonconvex optimization problems.

The solution algorithm for fluid flow calculations in a generalized curvilinear coordinate system is basically similar to the SIMPLER algorithm [9] which consists of solving a pressure equation to obtain the pressure field and solving a pressure-correction equation to correct predicted velocities. We took initial velocity and temperature to be zero.

We now lay the ground work for the computational study of this optimization problem We apply the *discrete Armijo gradient algorithm* [10]. It should be noted that the nonconvexity of the functionals implies that the convergence of such an algorithm is conditional, i.e., it depends on having a good "initial guess". We describe the algorithm in our current context; the search direction $\mathbf{h}_i$ is a finite difference approximation to $-\nabla \mathscr{J}$, with the parameter ε controlling the precision of this approximation.

The *discrete Armijo gradient algorithm* is a variable step size gradient method. It is particularly easy to implement since the step size selection does not require a one-dimensional line search. Convergence proofs under mild conditions on the functional are available [11]. In practice, we have found it to perform well, needing, on the average, approximately 15 iterations for satisfactory convergence but each iteration required five functional calculations in average. Of course, there are more sophisticated optimization methods available, e.g. trust-region quasi Newton methods. However, for our purposes, the *Armijo algorithm* was entirely adequate since our main goal in this study was to demonstrate the effectiveness of a systematic optimal control approach for improving processes such as Cz.

Discrete Armijo Gradient Algorithm

1. Choose $\alpha, \beta \in (0, 1)$, $\gamma \in (0, \infty)$ and k^*, $k_0 \in \mathscr{Z}$. Choose initial guesses for the control parameters Ha and ξ. Set $i = 0$ and $\varepsilon = \beta^{k_0}$.
2. Determine the search direction $\mathbf{h}_i$ having components

$$h_{i1} = -\frac{\mathscr{J}(\mathrm{Ha} + \varepsilon, \xi) - \mathscr{J}(\mathrm{Ha}, \xi)}{\varepsilon} \tag{31}$$

and

$$h_{i2} = -\frac{\mathscr{J}(\mathrm{Ha}, \xi + \varepsilon) - \mathscr{J}(\mathrm{Ha}, \xi)}{\varepsilon}. \tag{32}$$

3. Compute

$$\Delta_i = -\frac{\mathscr{J}(\mathrm{Ha} + \varepsilon h_{i1}, \xi + \varepsilon h_{i2}) - \mathscr{J}(\mathrm{Ha}, \xi)}{\varepsilon}. \tag{33}$$

4. If $\Delta_i > 0$, replace ε by $\beta\varepsilon$, and go to Step 1. Else, use the subprocedure given below, which requires k^*, to compute the step size $\lambda_i = \beta^{k_i}$, where $k_i \in \mathscr{Z}$, such that

$$\mathscr{J}(\mathrm{Ha} + \beta^{k_i} h_{i1}, \xi + \beta^{k_i} h_{i2}) - \mathscr{J}(\mathrm{Ha}, \xi) \leqslant \beta^{k_i} \alpha \Delta_i \tag{34}$$

and

$$\mathscr{I}(\mathrm{Ha} + \beta^{k_i-1}h_{i1}, \xi + \beta^{k_i-1}h_{i2}) - \mathscr{I}(\mathrm{Ha}, \xi) > \beta^{k_i-1}\alpha\Delta_i. \tag{35}$$

5. If $\mathscr{I}(\mathrm{Ha} + \lambda h_{i1}, \xi + \lambda h_{i2}) - \mathscr{I}(\mathrm{Ha}, \xi) > -\gamma\varepsilon$, replace ε by $\beta\varepsilon$, and go to Step 1. Else, replace Ha by Ha$+\lambda h_{i1}$, ξ and $\xi + \lambda h_{i2}$, and i by $i + 1$; then, go to Step 1.

Step size subprocedure

1. If $i = 0$, set $k' = k^*$. Else, set $k' = k_{i-1}$.
2. If $k_i = k'$ satisfied Eqs. (34) and (35), stop.
3. If $k_i = k'$ satisfies Eq. (34) but not Eq. (35), replace k' by $k' - 1$ and go to Step 2.
4. If $k_i = k'$ satisfied Eq. (35) but not Eq. (34), replace k' by $k' + 1$ and go to Step 2.

3.1. Simulation code

Over the past 25 years, transport phenomena in Cz crystal growth processes have been numerically simulated by many investigators; see, e.g., Refs. [12–16]. The simulation code used in our optimization studies is based on a high-resolution computer model developed in Refs. [6,17,18]. This model employs a multizone adaptive grid generation scheme and a curvilinear finite volume formulation. Once a grid has been generated for the flow domain, the control volume formulation begins by decomposing the domain into nonoverlapping control volumes such that there is one control volume surrounding each grid point. This computational domain also allows for the coexistence of various materials in different phases with significantly different thermophysical and transport properties. Next, the governing MHD equations are integrated over each control volume. Piecewise profiles expressing the variation of state variables between the grid points are then used to evaluate the required integrals. The end result is the discrete equations containing the values of the state variables for a group of grid points. The appealing feature of the control volume formulation is that the integral conservation of mass, momentum, and energy are satisfied exactly over any group of control volumes and, of course, over the whole computational domain. For more details on the finite volume formulation, see, e.g., Ref. [9].

4. Numerical results

In every case we studied, the optimal value of the side-wall temperature parameter turned out to be its limiting value $\xi = -1$. (Recall that we cannot allow $\xi < -1$ since this would cause the melt to solidify at the side wall.) This is not a surprising result in optimization, i.e., the optimal value of a parameter is at the boundary of its admissibility set. As a result, we will not provide results for optimization studies with respect to ξ. Instead, we give results for $\xi = 0$, i.e., a constant temperature profile, which is what was chosen in most past simulations, see, e.g., Refs. [6,7,19], and for $\xi = -1$, i.e., a linear temperature profile having as much slope as allowable, which provides the optimal results.

The CPU time for solving the partial differential equations in 100 time steps with 102×50 mesh is about 23 min on Linux computer which had a 600 MHz processor, Intel Pentium III with 256 MBytes memory.

For all the numerical experiments we describe here, we used 102×50 spacial grid and 100 time steps with a nondimensionalized time step $\delta t = 0.0005$; this corresponds to approximately 17 s. In fact, we did not see a significant change even we use 1000 time steps since we assume a quasi-state case. Otherwise, the melt drop will affect the heat transfer. For a silicon melt, we have the physical parameters $\sigma = 1.2 \times 10^6$ S/m (electrical conductivity), $v = 3.0 \times 10^{-7}$ m^2/s (kinematic viscosity), $\rho = 2420$ kg/m^3 (density), and $b = 0.1$ m; see Table 1 for more information. We assume that the magnetic field is in the axial direction, which is the most practical choice. The ambient temperature is such that $\Theta = -6.00372$; of course, $\Theta = 0$ and 1 corresponds to the freezing temperature of the melt and the constant temperature at the bottom of the crucible, respectively.

The crystal radius has been specified in the simulations. The pulling rates can be determined

Table 1
Thermophysical properties and parameters for Si melt and solid

Properties of Si melt		
Density	kg/m^3	2420
Thermal conductivity	W/mK	64
Kinematic viscosity	m^2/s	3.0×10^{-7}
Freezing temperature	°C	1410
Surface tension	N/m	0.72
Latent heat of solidification	J/kg	1.8
Coefficient of thermal expansion	/K	1.41×10^{-5}
Specific heat capacity	J/kg K	1000
Emissivity		0.15
Stefan number		8.33×10^{-2}
Properties of Si solid		
Density	kg/m^3	2300
Thermal conductivity	W/mK	22
Specific heat capacity	J/kg K	1000
Electrical conductivity	S/m	5.8×10^{4}
Emissivity		0.75
Grashof number		1.0×10^{6}
Prandtl number		15×10^{-3}
Stefan number		4.17×10^{-11}

Table 2
Objective functional values vs. Hartmann number for different iterations of the discrete Armijo gradient algorithm (above the line) and for some additional values of the Hartmann number above the optimal value (bold face) determined by that algorithm (below the line). The imposed temperature along the side wall of the crucible is a constant ($\xi = 0$)

Iteration no.	Hartmann no.	$\mathscr{I}_1$
1	100.00000	2121.056806
2	125.00000	1286.909470
3	133.00000	1143.171567
4	134.66505	1117.664065
5	134.98452	1113.226481
6	135.09339	1112.402257
7	135.11556	1112.379587
8	135.11132	1112.378560
9	**135.11178**	1112.378542
—	135.11200	1112.378545
—	136.12222	1169.954222
—	138.00000	1326.942849
—	140.00000	1532.767010
—	150.00000	4043.390458

based on the given radius. The pulling rates are small compared to the melt velocity.

4.1. Minimization of the vorticity functional $\mathscr{I}_1$

4.1.1. Constant temperature wall profile

For the choice $\xi = 0$, a constant side-wall temperature, we initially chose the parameters for the discrete Armijo gradient algorithm as follows: $\varepsilon = 0.01, k = 6, \beta^k = \varepsilon$, i.e., $\beta \approx 0.46, \alpha = 0.5, \gamma = 5$, and Ha = 100. Table 2 gives, for each optimization iteration, the value of the Hartmann number and the corresponding value of the functional $\mathscr{I}_1$. The optimization algorithm converged after nine iterations; the optimal value of the Hartmann number for this case is Ha = 135.1117816 which, for our choice of physical parameters, corresponds to an applied magnetic field of 0.0331 T; $u = 113.3$, velocity in axial direction, corresponds to 0.0003 m/s; $\mathrm{Re}_{\mathrm{cru}} = -500$, crucible rotation rate, corresponds to −0.0151/s. We also computed the value of the functional for values of the Hartmann number above the optimal value produced by the optimizer in order to show that the optimizer did indeed find a minimum of the functional. These results are also given in Table 2. In Fig. 3, we provide plots of the values of the logarithm of the functional and of the Hartmann number vs. the iteration number; these clearly show the convergence of the iterative method. In that figure, we also provide a plot of the value of the logarithm of the functional vs. the Hartmann number, where the latter is chosen to be the values visited during the optimization iteration and some additional values chosen after the iteration is completed. We clearly see that the optimizer did indeed find a minimum of the functional. In Figs. 4 and 5, we provide plots of the velocity vector and of its magnitude for no control applied, i.e., no applied magnetic filed (Ha = 0), and for the optimal magnetic field (Ha = 135.11178). Notice that convection in the melt is significantly reduced for the optimal value of Ha. In fact, the maximum magnitude of the velocity decreases from 694.547 for Ha = 0 to 27.6721 for the optimal value of Ha. In Figs. 4 and 5, we also provide contour plots of the temperature in the melt and the crystal.

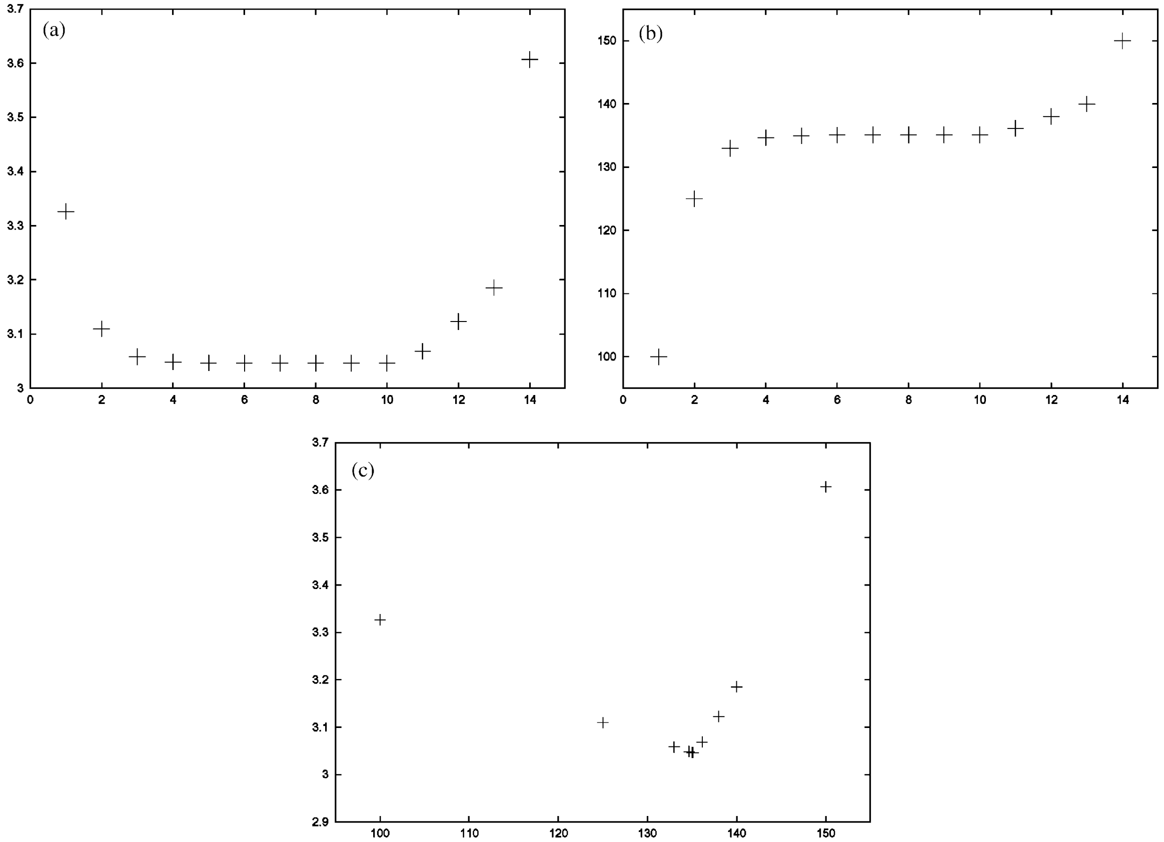

Fig. 3. Functional and Hartmann number values for a constant crucible side wall temperature profile ($\xi = 0$). (a) Value of the functional $\mathscr{I}_1$ vs. optimization iter. Number as determined by the optimization process (first nine points) and for some additional values of the Ha number (last five points). (b) Ha number vs. optimization iter. Number as determined by the optimization process (first nine points) and some additional values chosen to determine if the optimizer truly found a minimum (last five points). (c) Value of the logarithm of the functional $\mathscr{I}_1$ vs. Hartmann number showing the existence of a minimum. The values of the Ha number for the points plotted to the left of the minimum were determined by the optimization process; those to the right were chosen so as to show the minimum.

4.1.2. Optimal temperature wall profile

For the choice $\xi = -1$, the optimal linear sidewall temperature, we initially chose the parameters for the discrete Armijo gradient algorithm as follows: $\varepsilon = 0.001$, $k = 6$, $\beta^k = \varepsilon$, i.e., $\beta \approx 0.32$, $\alpha = 0.5$, $\gamma = 7$, and Ha = 10. After five iterations there was a need to change α to 0.86 and β to 0.35. Table 3 and Figs. 6–8 provide, for $\xi = -1$, the corresponding information that was provided for $\xi = 0$ in Table 2 and Figs. 3–5, respectively. The optimization algorithm converged after 21 iterations; the optimal value of the Hartmann number was now found to be Ha = 134.66505. Again, the convection in the melt is significantly reduced for the optimal value of Ha. In the Ha = 0 case, a large convective flow was observed in the melt and more specifically near the interface; for Ha = 134.66505, which was obtained by optimization, we see a greatly reduced convective flow. For $\xi = -1$, the maximum magnitude of the velocity decreases from 507.8 for Ha = 0 to 10.55 for the optimal value of Ha in Table 4. Of particularly interest are the results along the crystal interface; there the norm of velocity was reduced from 66 for Ha = 0 to 10.6 for the optimal value Ha = 134.66505.

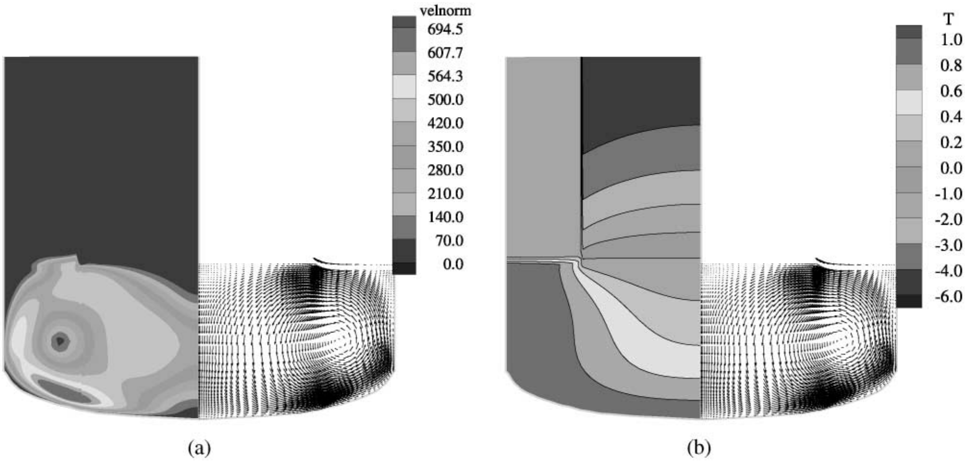

Fig. 4. Temperatures in the melt and crystal and velocities in the melt for a constant crucible side wall temperature profile ($\xi = 0$) and Ha = 0 (no magnetic control applied); (a) the left half gives the contours of the speed and the right half gives the velocity vector, (b) the left half gives the temperature and the right half gives the velocity vector.

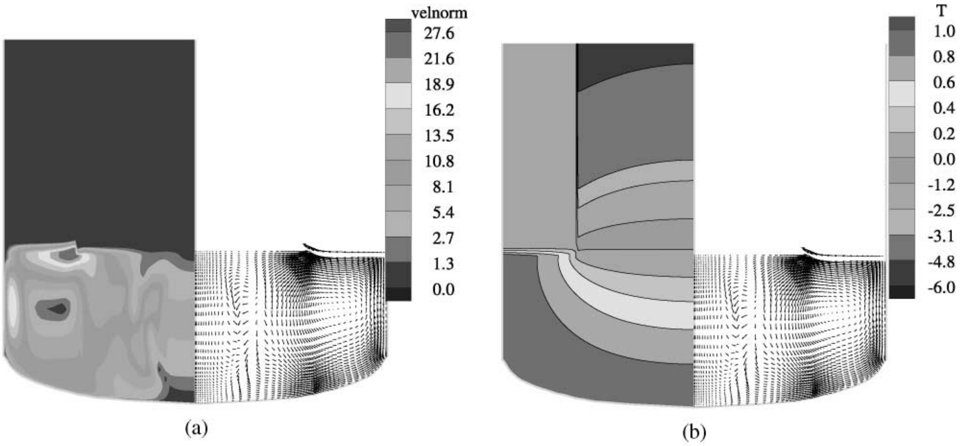

Fig. 5. Temperatures in the melt and crystal and velocities in the melt for a constant crucible side wall temperature profile ($\xi = 0$) and Ha = 135.11178 (the optimal value determined by the optimizer for the functional $\mathcal{J}_1$). (a) The left half gives the contours of the speed and the right half gives the velocity vector, (b) the left half gives the temperature and the right half gives the velocity vector.

4.1.3. Comparison of constant and linear wall temperature profiles

From Table 4 and Figs. 9 and 10, it is clear that the linear temperature profile (27) with $\xi = -1$ along the crucible wall yields better results, e.g., a greater suppression of convective perturbations in the melt. For example, from Table 4, we see that for Ha = 0 there is a reduction of the maximum speed of flow perturbations from 694.5 for the constant profile to 507.8 for the linear profile. For the corresponding optimal Hartmann numbers, the reduction is from 27.67 to 10.55. Plots of the velocity, stream function, and temperature for the constant and linear temperature crucible wall temperature profiles are given in Figs. 9 and 10. It is clear from the stream function contour plots that the stream function gradient has been reduced, which shows that convection in the melt has also been reduced; see Figs. 9a and 10a. From Table 4, we see that, for the corresponding optimal

Table 3
Objective functional values vs. Hartmann number for different iterations of the discrete Armijo gradient algorithm (above the line) and for some additional values of the Hartmann number above the optimal value (bold face) determined by that algorithm (below the line). The imposed linear temperature profile along the side wall of the crucible has maximum allowable slope ($\xi = -1$)

Iteration no.	Hartmann no.	$\mathcal{J}_1$
1	10.00000	49455.851095
2	34.30591	7510.535628
3	40.47653	4663.203345
4	51.09596	2378.748929
5	64.24992	1279.573829
6	80.41390	747.534616
7	100.96154	476.158066
8	109.16027	418.440560
9	115.15040	386.126853
10	119.97603	364.650641
11	124.05711	349.064600
12	127.61256	337.116627
13	130.77333	327.605411
14	133.62488	319.821284
15	134.53541	317.518290
16	134.62291	317.367216
17	134.63926	317.349610
18	134.65084	317.340238
19	134.65845	317.335694
20	134.66313	317.333594
21	**134.66505**	317.332895
—	136.22639	418.186535
—	138.92060	691.996673

values of the Hartmann number, the spread in the stream function is reduced from 1.86 for the constant temperature profile to 0.66 for the linear temperature profile.

4.1.4. *Effects of variations in the Hartmann number*

So far we have examined the effect of two design parameters, the Hartmann number corresponding to an applied axial magnetic field and the slope in the linear temperature along the crucible wall. We have seen that optimization with respect to either of these can result in a reduction in the perturbation velocity and the vorticity in the melt. We have also seen that variations in the Hartmann number can be much more effect than variations in the slope of the wall temperature profile. For example, at Ha = 0, going from constant wall temperature profile to the linear profile with maximum allowable slope effected a reduction in the velocity norm from 694.5 to 507.8. However, for each of these extremes in the slope of the wall temperature profile, much greater reductions can be effected by optimizing with respect to the Hartmann number. For the constant temperature profile ($\xi = 0$), the perturbation velocity norm was reduced from 694.5 at Ha = 0 to 27.67 at the optimal value Ha = 135.11178 and for the best linear temperature profile ($\xi = -1$), the perturbation velocity norm was reduced from 507.8 at Ha = 0 to 10.55 at the optimal value Ha = 134.66505.

The effects of variations in the Hartmann number for the optimal linear wall temperature profile is illustrated in the bottom plots of Figs. 7 and 8 where the temperature is plotted for Ha = 0 and the optimal value Ha = 134.66505. From these plots, it is clear that the magnetic field has a smoothing and stabilizing effect on the temperature distribution in the melt.

4.1.5. *Effects of other design parameters*

There are a number of other design parameters that may be used in attempting to reduce velocity and vorticity perturbations in the melt. For example, two that have been suggested are the crucible and crystal rotation rates. Before using these parameters in our sophisticated optimization methodology, we examined how variations in their values affected the velocity perturbations in the melt. Variations in the Hartmann number have a large effect on the maximum and minimum values of the velocity components. However, variations in the crucible and crystal rotation rates seem to have no effect on the velocity perturbations. Thus, these are not effective design parameters to use if one wants to suppress velocity perturbations in the melt.

4.2. *Minimization of temperature gradient functionals $\mathcal{J}_2$ in melt and $\mathcal{J}_3$ in crystal near interface*

We have observed how some design parameters (e.g., the Hartmann number) are very effective in reducing velocity perturbations in the melt, others

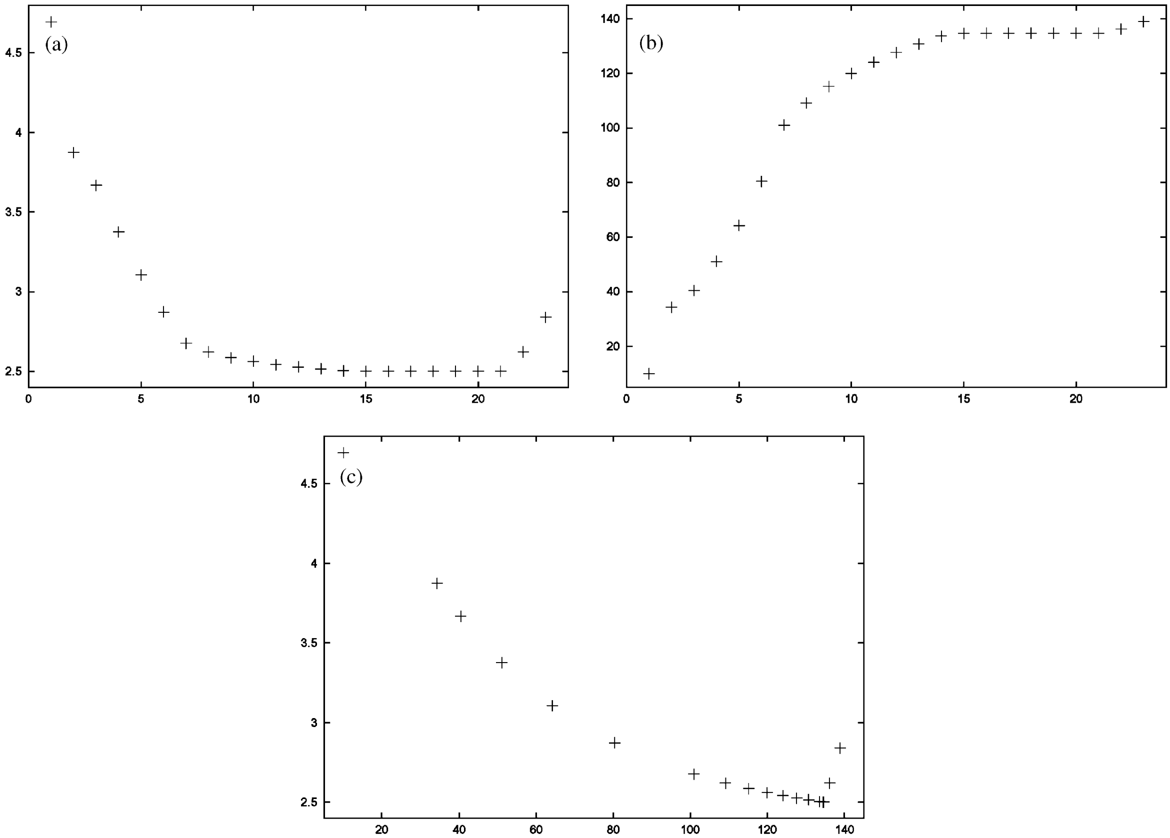

Fig. 6. Functional and Hartmann number values for the optimal linear crucible side wall temperature profile ($\xi = -1$). (a) Value of the functional $\mathscr{J}_1$ vs. optimization iteration number as determined by the optimization process (first 21 points) and for some additional values of the Ha number (last two points). (b) Ha number vs. optimization iteration number as determined by the optimization process (first 20 points) and some additional values chosen to determine if the optimizer truly found a minimum (last two points). (c) Value of the functional $\mathscr{J}_1$ vs. Ha number showing the existence of a minimum. The values of the Ha number for the points plotted to the left of the minimum were determined by the optimization process; those to the right were chosen so as to show the minimum.

are mildly effective (e.g., the slope of a linear temperature profile along the wall of the crucible), while others are very ineffective (e.g., the crucible and crystal rotation rates.) We now want to see how effective these parameters are in reducing temperature gradients in the melt, i.e., for the minimization of the functional $\mathscr{J}_2$, and in the crystal, i.e., for the minimization of the functional $\mathscr{J}_3$. Again, before using these parameters in our sophisticated optimization methodology, we examined how variations in the values of the design parameters affect the functionals $\mathscr{J}_2$ and $\mathscr{J}_3$. A sampling of results is given in Table 5. We see that variations in the Hartmann number and the crucible and crystal rotation rates have almost no appreciable effect on the values of $\mathscr{J}_2$ and $\mathscr{J}_3$ which are root-mean-square measures of the temperature gradient. However, variations in the control parameters can effect some reductions in the *maximum* value of the temperature gradient and in the values at specific points and subregions such as in the triple point where the crystal, melt and encapsulant meet and the areas near the crystal/melt interface. Therefore, optimization of functionals such as $\mathscr{J}_2$ and $\mathscr{J}_3$ is ineffective for reducing temperature gradients in the crystal. This

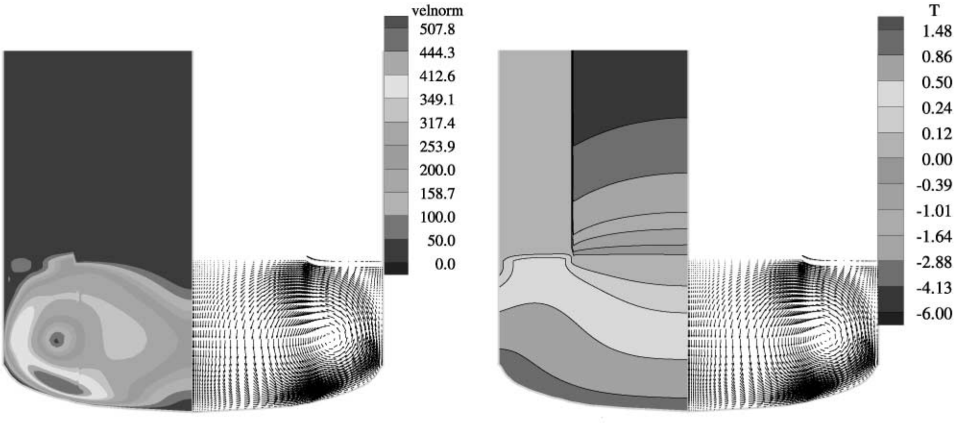

(a) (b)

Fig. 7. Temperatures in the melt and crystal and velocities in the melt for optimal linear crucible side wall temperature profile ($\xi = -1$) and Ha = 0 (no magnetic control applied) (a) the left half gives the contours of the speed and the right half gives the velocity vector, (b) the left half gives the temperature and the right half gives the velocity vector.

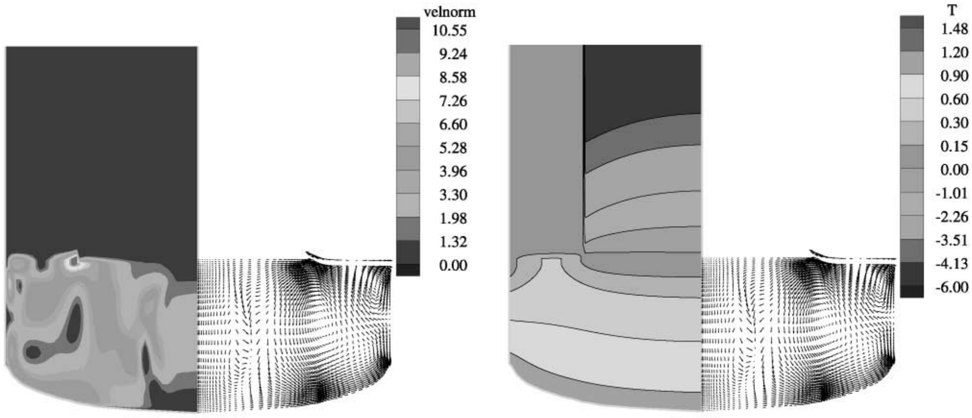

(a) (b)

Fig. 8. Temperature in the melt and crystal and velocities in the melt for optimal linear crucible side wall temperature profile ($\xi = -1$) and Ha = 134.66505 (the optimal value determined by the optimizer for the functional $\mathscr{I}_1$). (a) The left half gives the contours of the speed and the right half gives the velocity vector, (b) the left half gives the temperature and the right half gives the velocity vector.

Table 4
Maximum and minimum melt flow temperature and stream function values and maximum speed for no applied magnetic field and for the optimal values (with respect to the functional $\mathscr{I}_1$) of the applied field strength and for constant ($\xi = 0$) and best linear crucible wall temperature profiles ($\xi = -1$)

Hartmann no.	Temperature			Stream function		Max speed
	Wall profile	Min	Max	Min	Max	
0	Constant	−6.003	1.0	−86.81	0.59	694.5
0	Linear	−6.003	1.484	−64.24	2.92	507.8
135.11178	Constant	−6.003	1.0	−1.864	0.0	27.67
134.66505	Linear	−6.003	1.484	−0.665	0.309	10.55

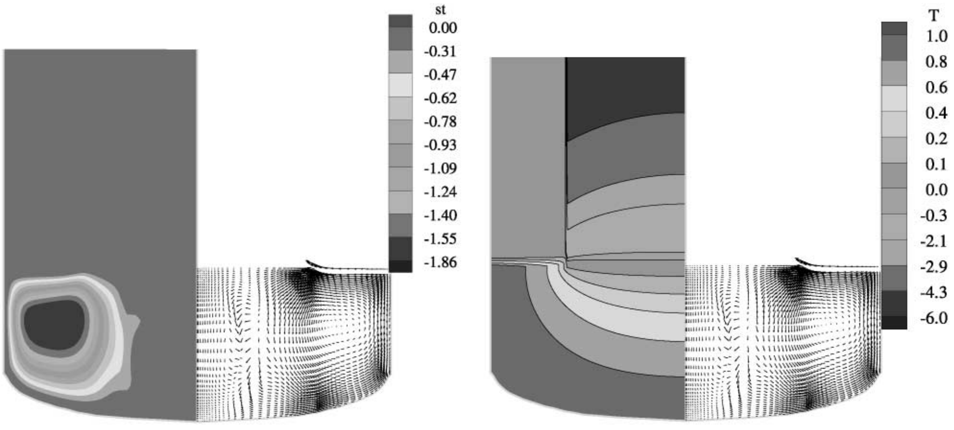

(a) (b)

Fig. 9. Stream function and velocity in the melt and temperature in the crystal and melt for the optimal values of the Hartmann number determined by the minimization of the functional $\mathcal{I}_1$ and $\xi = 0$ (a constant crucible side wall temperature profile), (a) the left half gives the contours of the stream function and the right half gives the velocity vector, (b) the left half gives the temperature and the right half the velocity vector.

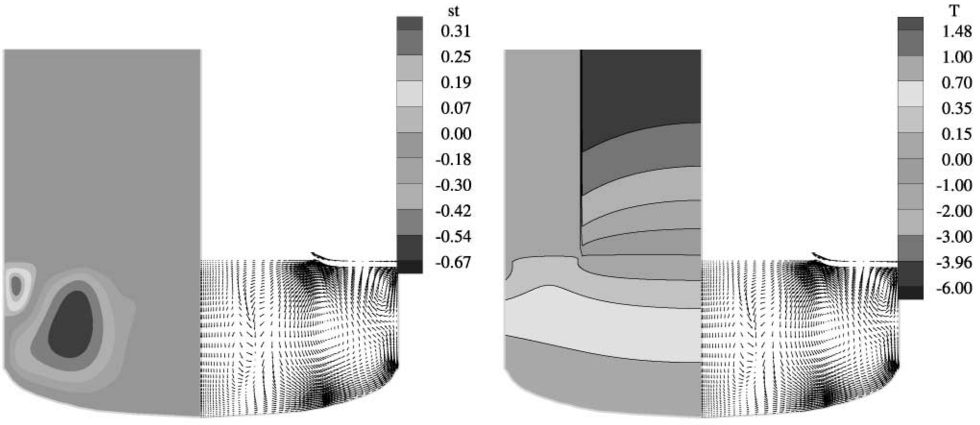

(a) (b)

Fig. 10. Stream function and velocity in the melt and temperature in the crystal and melt for the optimal values of the Hartmann number determined by the minimization of the functional $\mathcal{I}_1$ and $\xi = -1$ (a constant crucible side wall temperature profile), (a) the left half gives the contours of the stream function and the right half gives the velocity vector, (b) the left half gives the temperature and the right half the velocity vector.

is due to the small value of the Prandtl number. Recall that the Prandtl number is the ratio of the momentum and thermal diffusivities, i.e., it is a measure of the relative size of the momentum transport and conductive heat transfer effects. We should point out that in the crystal region there were other local maxima of the temperature gradient in regions for away from the melt region; these values were very insensitive to changes in parameter values.

Table 5
Maximum temperature gradient in melt and crystal and functional values in melt $\mathscr{I}_2$ and crystal $\mathscr{I}_3$ for several values of the Hartman number and of the crystal and crucible rotation Reynolds numbers

Hartmann no.	Crucible rotation rate	Crystal rotation rate	$\lvert\nabla T\rvert^2_{\max}$		Functional value	
			In melt	In crystal	In melt	In crystal
0	0	1000	39.3172	2.21426	0.06796	15.25665
	−500	0	38.5130	2.2693	0.06631	15.25669
	−500	2000	36.1654	2.2252	0.06692	15.25668
	−1000	1000	39.5406	2.3522	0.06645	15.25668
	−3000	1000	38.7061	2.3035	0.06669	15.25667
30	0	1000	35.8517	2.0597	0.06479	15.25671
	−500	0	37.9086	2.2316	0.06484	15.25670
	−500	2000	36.1654	2.2252	0.06692	15.25668
	−1000	1000	37.8650	2.2155	0.06478	15.25671
	−3000	1000	37.1574	2.1715	0.06498	15.25669
134.66504	0	1000	35.3139	2.0896	0.06439	15.25674
	−500	0	35.9296	2.1215	0.06439	15.25673
	−500	2000	33.9489	2.0307	0.06440	15.25674
	−1000	1000	35.4594	2.0883	0.06439	15.25673
	−3000	1000	34.8467	2.0454	0.06441	15.25672
150	0	1000	35.2913	2.0884	0.06440	15.25674
	−500	0	35.8170	2.1156	0.06439	15.25673
	−500	2000	34.0652	2.0344	0.06440	15.25674
	−1000	1000	35.3645	2.0854	0.06439	15.25673
	−3000	1000	34.8196	2.0473	0.06441	15.25672
199	0	1000	35.2751	2.0852	0.06446	15.25674
	−500	0	35.4982	2.0974	0.06446	15.25673
	−500	2000	34.4264	2.0474	0.06446	15.25674
	−1000	1000	35.2657	2.0804	0.06446	15.25673
	−3000	1000	34.5574	2.0375	0.06446	15.25672

5. Concluding remarks

In this paper, our goal has been to demonstrate some of the techniques being used to develop an integrated approach for intelligent modelling, design and control of crystal growth processes. This is a challenging task; however, the potential benefits are large. Our current thrust has been on developing control and optimization algorithms that can be implemented into existing codes for the MCz crystal growth process. Carrying out this goal has involved an integration between the experiments, modeling, simulations and control experts and results.

In our studies we have shown how the choices of design parameters and objective functional can have a drastic effect on the success of an optimization or control strategy. For example, we have shown that optimization with respect to the slope of a linear temperature profile along the crucible wall has a mild effect on the size of velocity and vorticity perturbations in the melt. On the other hand, drastic reductions can be effected by optimizing with respect to the strength of an applied axial magnetic field and a negligible effect is realized by optimizing with respect to crucible and crystal rotation rates. This illustrates how, for a specific design objective, optimization with respect to some design parameters is much more effective than with respect to others.

We have also shown that although optimization with respect to the Hartmann number can drastically reduce the size of velocity and vorticity perturbations in the melt, it has negligible effect on the size of the temperature gradient in the crystal. This illustrates how the same design parameter has little influence on some functionals and great influence on others.

Current and future work includes the refinement and further development of practical control and optimization strategies; the integration of our results and algorithms into the latest version of MASTRAPP3d which simulates three dimensional MCz crystal growth processes; and the experimental verification and system integration of the control and optimization results obtained through computations.

References

[1] Y.T. Chan, H.J. Gibeling, H.L. Grubin, J. Appl. Phys. 64 (1988) 1425.

[2] K.M. Kim, G.H. Schwuttke, P. Smetana, IBM Tech. Disclosure Bull. 24 (1981) 3376.

[3] L.D. Landau, E.M. Lifshitz, Fluid Mechanics, Pergamon, London, 1959.

[4] J.S. Turner, Buoyancy Effects in Fluids, Cambridge, New York, 1973.

[5] S. Pai, Modern Fluid Mechanics, van Nostrand Reinhold, New York, 1981.

[6] H. Zhang, V. Prasad, Multizone adaptive simulations for high pressure crystal growth, Proc. ASME/JSME Therm. Eng. J. Conf., Maui, HI, 1995, pp. 559–568.

[7] V. Prasad, H. Zhang, A.P. Anselmo, Transport phenomena in Czochralski crystal growth processes, in: Advances in Heat Transfer, Vol. 30, Academic Press, New York, 1997, pp. 313–435.

[8] P.K. Moore, J.E. Flaherty, BIT Numer. Math. 33 (2) (1993) 309.

[9] S.V. Patankar, Numerical Heat Transfer and Fluid Flow, McGraw-Hill, New York, 1980.

[10] E. Polak, Optimization, Springer-Verlag, New York, 1997.

[11] L. Armijo, Pacific J. Math. 16 (1) (1966) 1.

[12] R.A. Brown, AIChE J. 43 (6) (1988) 881.

[13] S.H. Chan, D.H. Cho, G. Kocamustafaogullari, Int. J. Heat Mass Transfer 26 (4) (1983) 621.

[14] D.T.J. Hurle, B. Cockayne, Czochralski growth, in: D.T.J. Hurle (Ed.), Handbook of Crystal Growth, Vol. 2a, North-Holland, New York, 1994, pp. 99–211.

[15] G. Muller, Convection and inhomogeneities in Crystal growth from melt, in: H.C. Freyhardt (Ed.), Crystals, Vol. 12, (1988), Springer-Verlag, Berlin.

[16] V. Prasad, H. Zhang, Cryst. Growth Novel Electron. Mater. Cer. Trans. 60 (1995) 3.

[17] H. Zhang, M.K. Moallemi, Numer. Heat Transfer Part B 27 (1995) 255.

[18] H. Zhang, V. Prasad, M.K. Moallemi, Numer. Heat Transfer, Part B 29 (4) (1996) 399.

[19] P.J. Prescott, F.P. Incorpera, J. Heat Transfer 115 (1993) 302.